Supplement of

Dataset of airborne measurements of aerosol, cloud droplets and meteorology by tethered balloon during PaCE 2022

Viet Le[1], Konstantinos Doulgeris[1], Mika Komppula[1], John Backman[1], Gholamhossein Bagheri[2], Eberhard Bodenschatz[2], and David Brus[1]

[1]Finnish Meteorological Institute, Helsinki, FI-00560, Finland
[2]Max Planck Institute for Dynamics and Self-Organization, Am Fassberg 17, 37077 Göttingen, Germany

Correspondence: Viet Le (viet.le@fmi.fi)

S1 Sampling and transport losses calculations

Aerosol sampling and transport losses were calculated with help of Particle Loss Calculator (von der Weiden et al., 2009) for POPS, CPC and mCDA separately, since they were using their own inlets.

The CPC setup used horizontal sampling with a flow rate of 0.7 L min^{-1}. The sampling tube was 10 cm long with an inner diameter of 4 mm, and the instrument sampled aerosols in the 0.01 to 1 µm size range. The average wind speed during the measurements was 7 $\mathrm{m\,s}^{-1}$, with an aspiration angle of 0°. Aerosol sampling efficiency increased from 100% for 10 nm particles to 107% for 1 µm particles, due to sub-isokinetic sampling. Aerosol transport losses were up to 4% for 10 nm, 1% for 30 nm, and 0.1% for particles between 100 nm and 1 µm. In the worst-case scenario, with an aspiration angle of 90° (perpendicular to the wind direction), aerosol sampling efficiency increased from 100% for 10 nm to 104% for 1 µm particles.

The POPS setup used horizontal sampling with a flow rate of 0.181 L min^{-1}. The sampling tube was 5 cm long with an inner diameter of 2 mm, and the instrument sampled aerosols in the 0.15 to 3.5 µm size range. The average wind speed during the calculation was 7 $\mathrm{m\,s}^{-1}$, with an aspiration angle of 0° (into the wind direction). Aerosol sampling efficiency increased exponentially, from 100% for 0.15 µm particles to 150% for 3.5 µm particles, due to sub-isokinetic sampling. Aerosol transport losses were up to 1% for particles up to 2 µm, and up to 3% for particles between 2 and 3.5 µm. In the worst-case scenario, with an aspiration angle of 90° (perpendicular to the wind direction), sampling efficiency was slightly below 100% (ranging from 95% to 99%) for particles up to 1.9 µm, then decreased sharply and linearly, reaching 42% for 3.5 µm particles.

The mCDA setup used a vertical inlet with downward sampling at a flow rate of 2.8 L min^{-1}. The inlet was 10 cm long with an inner diameter of 8 mm, and the instrument sampled aerosol and cloud droplets in the 0.5–50 µm size range. Although the inlet is vertical, strong wind can induce tilting to the payload, potentially influencing the measurements. To assess this effect, two aspiration angles relative to the wind direction were evaluated, with wind speeds varying from 10 $\mathrm{m\,s}^{-1}$ down to 1 $\mathrm{m\,s}^{-1}$ in 1 $\mathrm{m\,s}^{-1}$ steps. Figure S1 shows the sampling efficiency for an aspiration angle of 90°. At a wind speed of 10 $\mathrm{m\,s}^{-1}$, particles larger than 5 µm are almost entirely not sampled, whereas at 1 $\mathrm{m\,s}^{-1}$ the cut-off diameter increases to approximately 12 µm.

Figure S2 shows the sampling efficiency for an aspiration angle of 45°. At a wind speed of $10\ \mathrm{m\ s^{-1}}$, the cut-off diameter is about 16 µm while at $1\ \mathrm{m\ s^{-1}}$ the mCDA can theoretically sample the full size range. However, the sampling efficiency drops below 15% for droplets bigger than 20 µm.

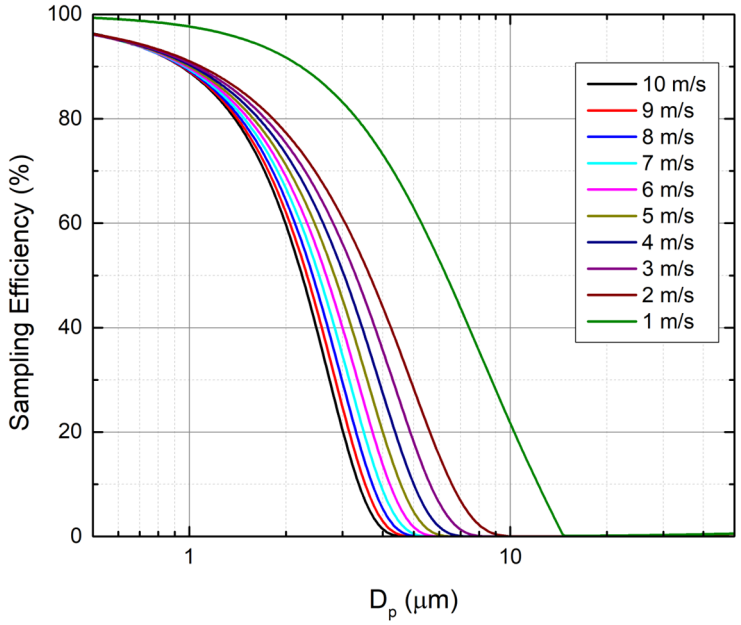

Figure S1. Sampling efficiency of mCDA calculated for different wind speeds and aspiration angle 90°.

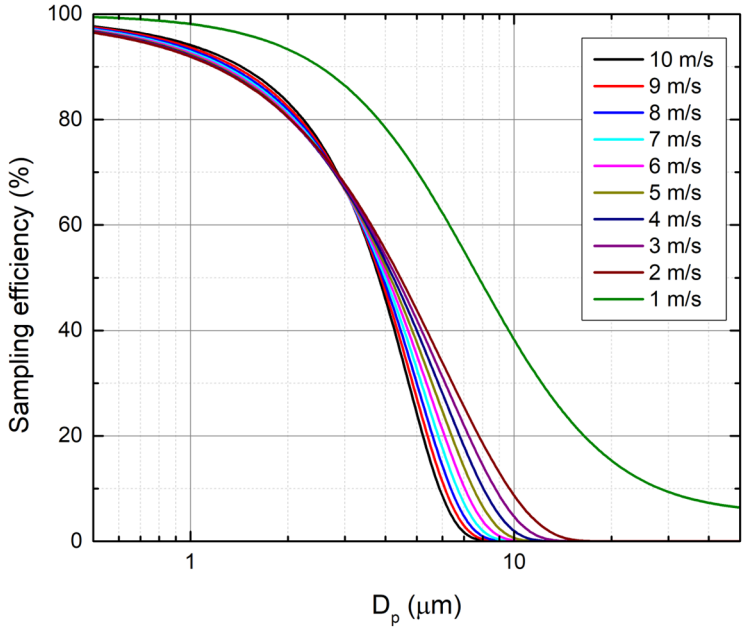

Figure S2. Sampling efficiency of mCDA calculated for different wind speeds and aspiration angle 45°.

S2 BME intercomparison

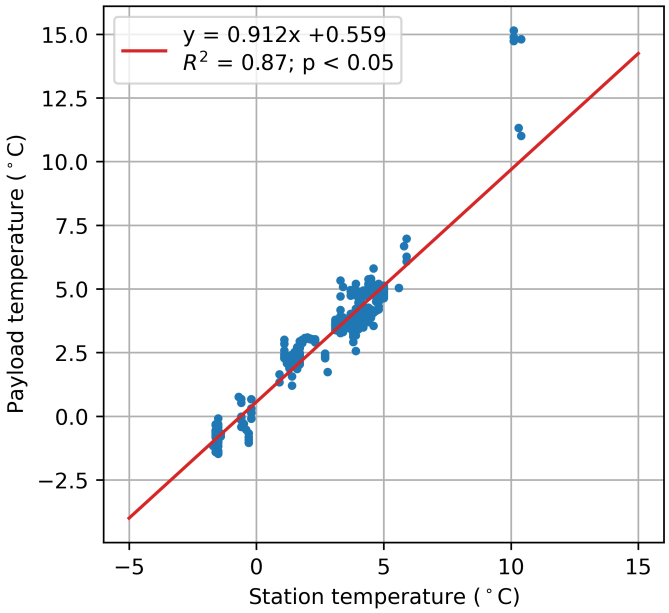

Figure S3. Intercomparison of temperature measurements from the BME sensor on the FMI balloon payload and the Vaisala Automatic Weather System at the Sammaltunturi station during the campaign (Backman et al., 2025). Balloon measurements were height matching the station within ±40 m.

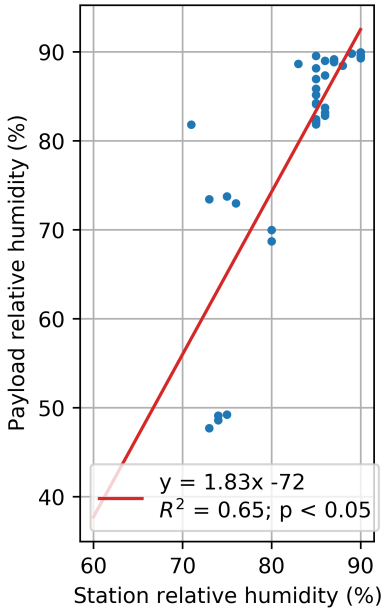

Figure S4. Intercomparison of relative humidity measurements from the BME sensor on the FMI balloon payload and the Vaisala Automatic Weather System at the Sammaltunturi station during the campaign (Backman et al., 2025). Balloon measurements were height matching the station within ±40 m. Only out-of-cloud relative humidity values below 90% are included.

S3 CPC calibration and intercomparison

Table S1. D_{50} counting efficiency measurement at different sets of TED. Scanning Mobility Particle Sizer (SMPS; model 3938, TSI Inc.) and a CPC (model 3776, TSI Inc.) were used to cut the polydisperse aerosol (ammonium sulfate) and as a reference for particle counting. CPC1 was onboard the FMI payload and operated with TED = 2000 mV during the campaign. CPC2 was used as a backup instrument in case of CPC1 failure.

CPC	D_{50} **mean (nm)**	**Std (nm)**	**16th pct (nm)**	**84th pct (nm)**
		TED = 1000		
CPC1	22.18	0.049	22.13	22.23
CPC2	21.08	0.040	21.04	21.13
		TED = 1500		
CPC1	15.43	0.039	15.39	15.47
CPC2	13.06	0.057	13.01	13.01
		TED = 2000		
CPC1	10.80	0.076	10.72	10.87
CPC2	9.91	0.098	9.82	9.99

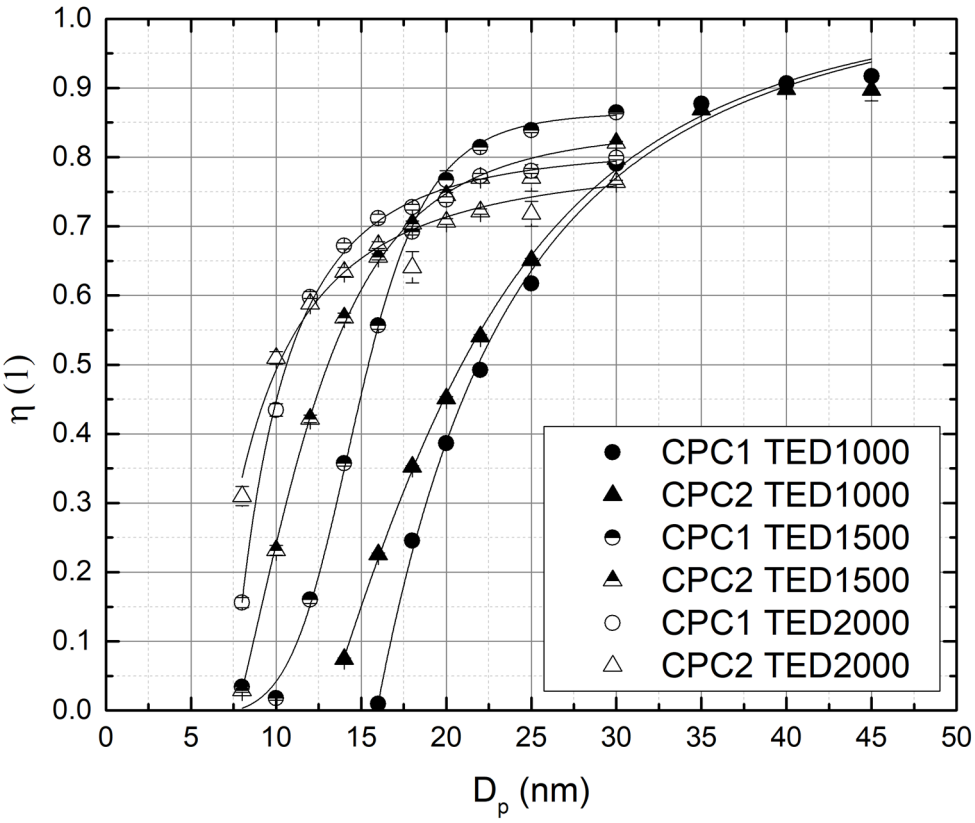

Figure S5. Counting efficiency D_{50} of CPC1 and CPC2 for diameters between 5 and 45 nm when operated at 1000, 1500 and 2000 mV TED voltages. CPC1 was onboard the FMI payload and operated with TED = 2000 mV during the campaign.

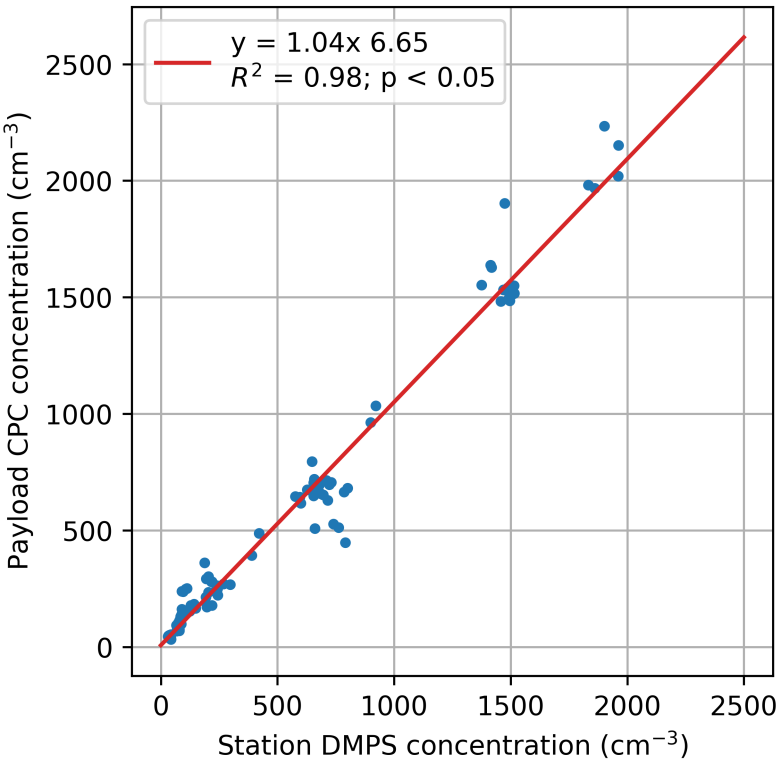

Figure S6. Intercomparson between the FMI balloon payload CPC measurement and the Sammaltunturi station's DMPS data from interstitial inlet during the campaign (Backman et al., 2025). The size range of DMPS is from 10 to 800 nm. Balloon measurements were height matching the station within ±40 m.

S4 POPS calibration

Table S2. Counting efficiency of two POPS instruments (SN:150 and SN:151) for diameters between 70 and 300 nm. Scanning Mobility Particle Sizer (SMPS; model 3938, TSI Inc.) and a CPC (model 3776, TSI Inc.) were used to cut the polydisperse aerosol (ammonium sulfate) and as a reference for particle counting. POPS 150 was onboard the FMI payload.

Instrument	$D_{50,\text{nominal}}$ **(nm)**	$D_{50,\text{MC mean}}$ **(nm)**	**Std (nm)**	**q16 (nm)**	**q84 (nm)**	**q2.5 (nm)**	**q97.5 (nm)**
POPS 150	141.33	141.32	0.56	140.78	141.87	140.18	142.40
POPS 151	139.37	139.42	1.39	137.99	140.91	137.00	142.17

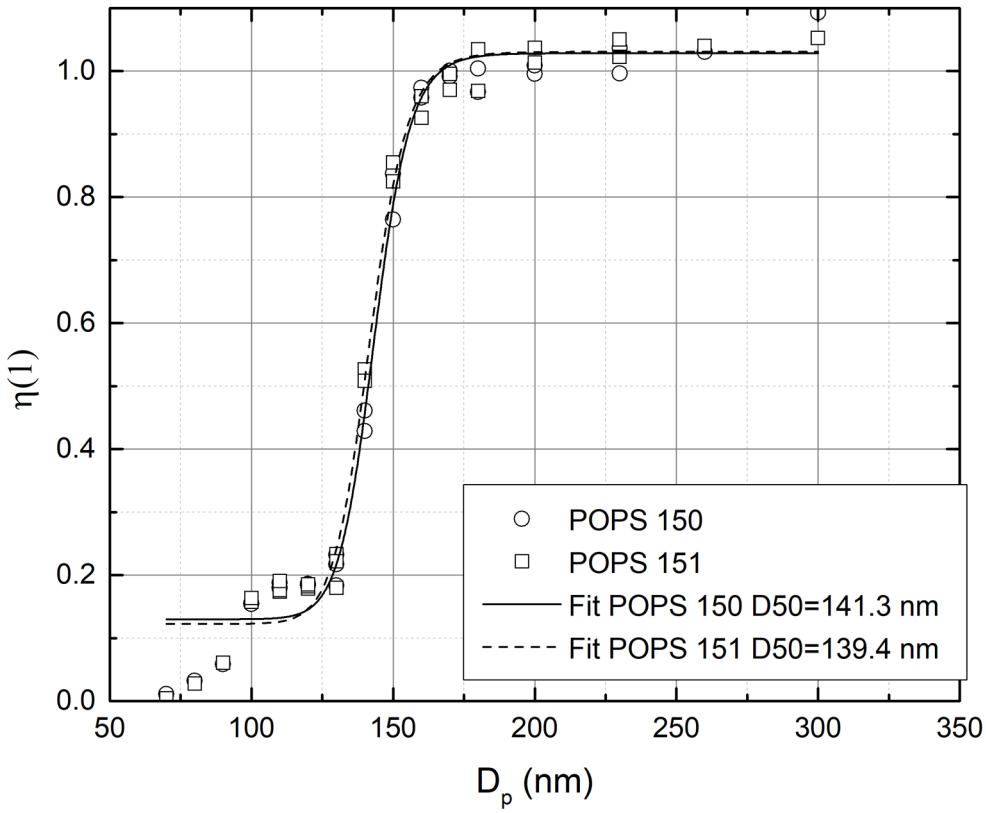

Figure S7. Counting efficiency of two of two POPS instruments (150 and 151) for diameters between 70 and 300 nm. Fitting curves were obtained using Monte Carlo simulations to determine the cut-off diameter D_{50}. POPS 150 was onboard the FMI payload.

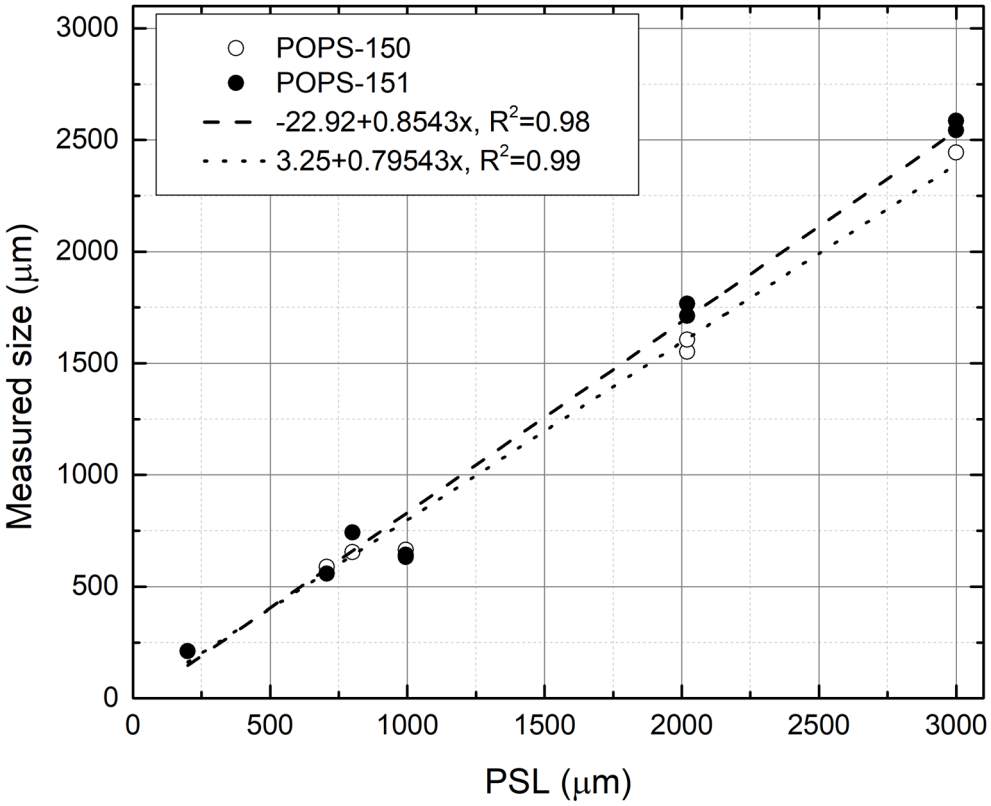

Figure S8. PSL calibration for POPS-150 and POPS-151. POPS-150 was onboard the FMI payload.

S5 Experimental determination of box temperature and relative humidity under various ambient conditions

To evaluate the sampling conditions for the CPC and POPS inside the FMI payload, three experiments were conducted: two under sub-zero ambient temperatures and one above zero, all with moderate wind speeds.

Table S3. Ambient conditions during box temperature experiments.

Case	Ambient temperature (°C)	Average wind speed (m s^{-1})	Max wind speed (m s^{-1})
1	-1.9 ± 0.3	2.1 ± 1.1	3.2 ± 1.4
2	5.1 ± 1.0	3.5 ± 1.1	6.7 ± 2.1
3	-6.2 ± 0.5	2.6 ± 0.6	4.2 ± 0.9

The payload had a setup similar to that used during the campaign. It consisted of a Styrofoam box (2.5 cm wall thickness, 0.026 m^3 volume) containing a CPC, a POPS, a Raspberry Pi 4 microcomputer, and a 4S Li-ion battery (8 Ah, 14.8 V). The inside box temperature (T) and relative humidity (RH) were simultaneously measured by a HYT271-S sensor (B+B Thero-Technik GmbH) and POPS internal housekeeping temperature. The CPC does not provide any information on the conditioning of the sample flow. The ambient temperature, relative humidity and wind were measured with Vaisala weather station model WXT520.

Figure S9 a shows the timeline of inside box temperature development; temperatures are continuously rising and, in about 45 minutes, reach the plateau and remain flat during the remaining length of the experiment. The difference between the measured temperatures is smaller when there is a lower ambient temperature, see Fig. S9 b. The temperature gradient between ambient and inside box temperature (20°C) leads to significant drop in measured RH inside the box, see Fig. S9 c and d.

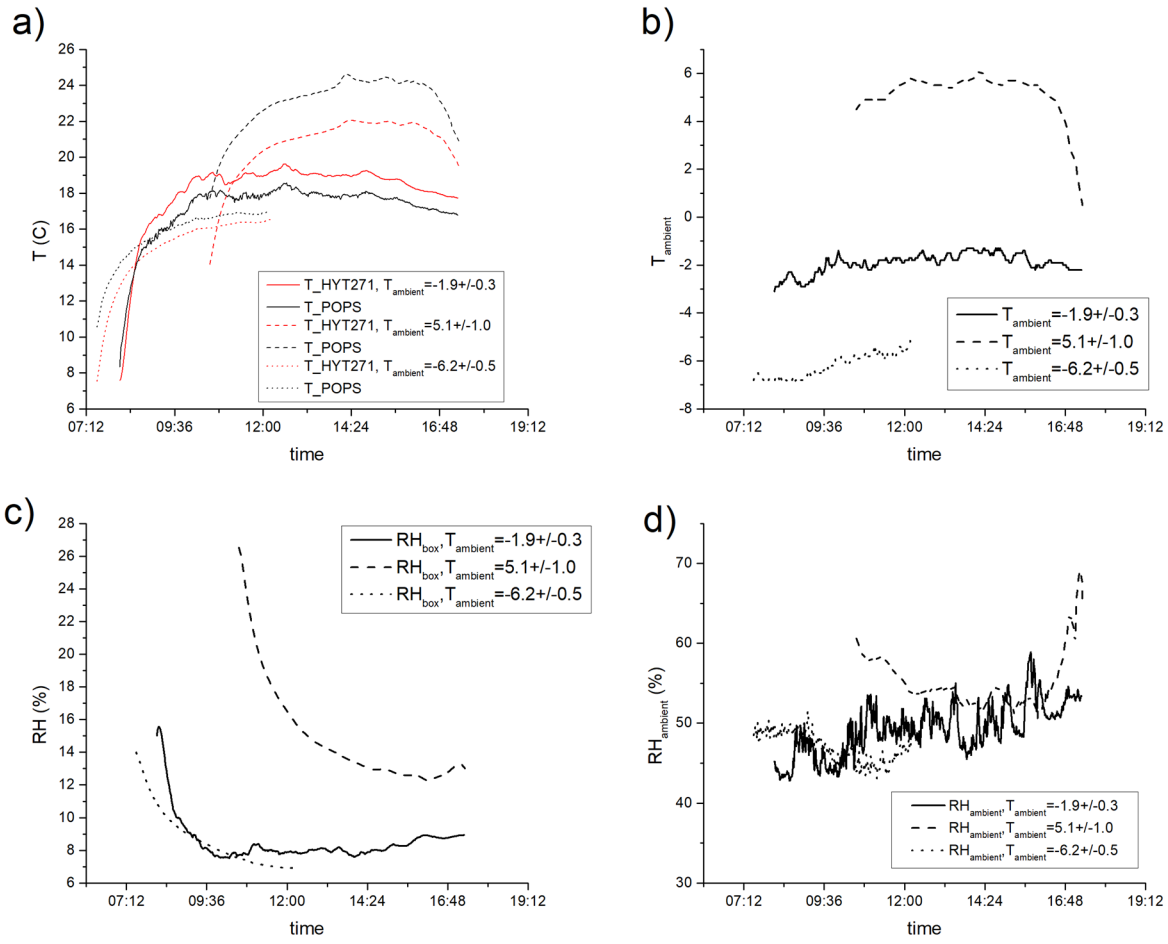

Figure S9. a) Temperature measured inside the box with HYT271 sensor and POPS inlet temperature, b) Ambient temperature measured with Vaisala WXT520, c) Relative humidity measured inside the box with HYT271 sensor, d) Ambient RH measured with Vaisala WXT520.

S6 mCDA intercomparison

Figure S10 displays the equivalent effective diameter (ED) measured in-flight by the mCDA onboard the FMI payload during selected balloon profiling cases, alongside measurements from the Cloud Droplet Analyzer (CDA, Palas GmbH) (Doulgeris et al., 2025) at the Sammaltunturi station over the same period. As the payload ascends through the clouds, the ED increases. In all cases, the ED measured at the station aligns with the ED measured by the balloon at comparable heights, although the station data exhibit considerably less variability than the balloon measurements.

It should be noted that the station and the balloon sampling location are separated by approximately 6 km. Consequently, the clouds sampled by the airborne payload and those observed at the station may not correspond to the air mass. Even if the wind directions were aligned with both the station and the payload (southwesterly or northeasterly), the time lags associated with wind speed, along with the spatial and temporal inhomogeneity of the clouds, further complicate direct comparisons. Therefore, differences in cloud microphysical structure and droplet size distributions between the two locations are expected.

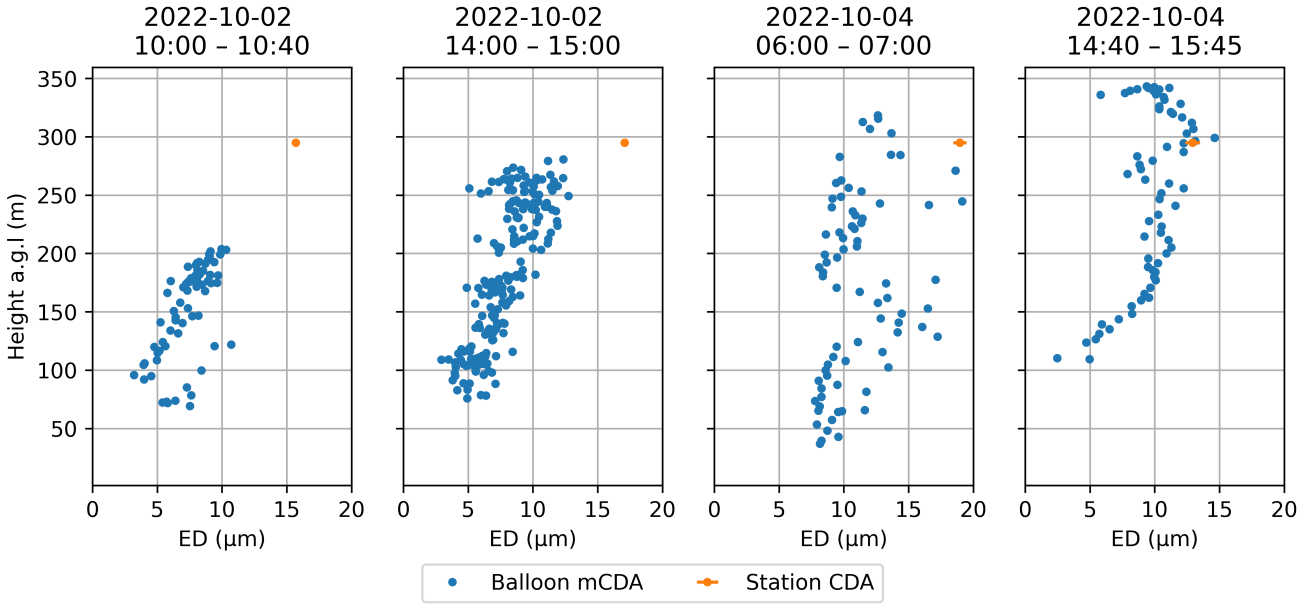

Figure S10. Comparison of the ED measured in-flight by the mCDA payload during selected balloon profiling cases and the CDA at the Sammaltunturi station over the same period. The time is in UTC.

As part of the ACTRIS Cloud In Situ (ACTRIS-CIS) ECCINT-INT01 campaign, the mCDA and CDA instruments participated in a ground-based intercomparison of cloud spectrometers conducted at the Sonnblick Observatory (3,106 m a.s.l.) from 21 November to 3 December 2022. This campaign, conducted right after the PaCE 2022 campaign, aimed to evaluate the performance of various cloud microphysical instruments under subzero atmospheric conditions.

Figure S11 shows the comparison of cloud droplet number concentration (N_c) measured by the mCDA and CDA during periods when the Sonnblick Observatory station was in-cloud. A clear correlation is observed, with the mCDA generally reporting higher number concentrations. Differences in N_c are attributed to instrument-specific inlet and sampling characteristics, as well as the known sensitivity of number concentration measurements to flow conditions and wind speed (Doulgeris et al., 2020, 2026).

Figure S12 shows the comparison of equivalent diameter (ED) measurements between the mCDA and the CDA. The measurements exhibit strong agreement and closely follow the 1:1 line over the full ECCINT-INT01 campaign period, indicating consistent droplet sizing by both instruments. Both the CDA and the mCDA sampled vertically during the intercomparison, an orientation known to introduce gravitational and inertial losses, particularly for larger cloud droplets (Doulgeris et al., 2025). These losses primarily affect cloud droplet number concentrations, while the derived ED and mean volume diameter are not significantly affected.

Overall, the intercomparison confirms that the mCDA provides reliable cloud droplet sizing and captures physically meaningful variability in number concentration, despite the known uncertainties associated with inlet orientation and sampling conditions. A more detailed analysis of the ECCINT-INT01 campaign results is presented in Doulgeris et al. (2026).

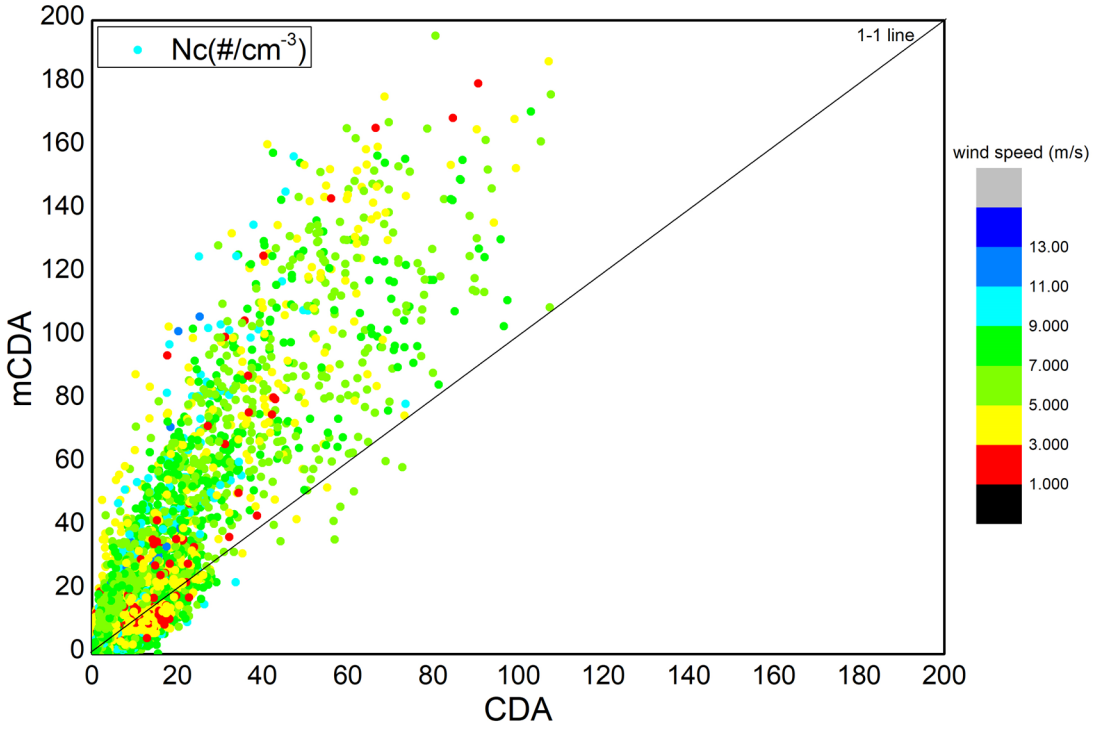

Figure S11. Comparison of one-minute averaged N_c derived from the mCDA and CDA during the ECCINT-INT01 intercomparison campaign, restricted to periods when the station was in cloud. Points are colored by ambient wind speed. The solid line indicates the 1:1 relationship.

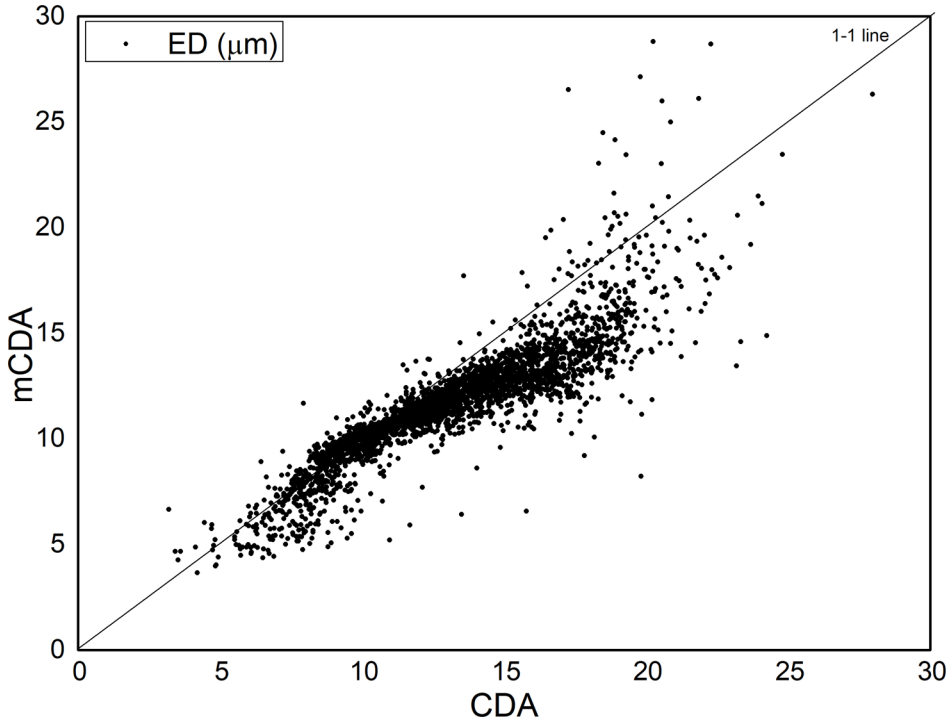

Figure S12. Comparison of one-minute averaged ED derived by the mCDA and CDA during the ECCINT-INT01 intercomparison campaign, restricted to periods when the station was in cloud. The solid line indicates the 1:1 relationship.

S7 Effects of payload orientation and wind speed

In this section, we examine the effects of payload orientation and wind on aerosol measurements. In the FMI payload configuration, the mCDA is equipped with a vertical inlet, whereas the POPS and CPC use horizontal inlets. Consequently, the influence of payload orientation and wind is expected to be more pronounced for the POPS and CPC than for the mCDA.

The CPC and mCDA operate with assumed (not measured) constant nominal sample flow rates (0.7 lpm for CPC and 2.8 lpm for mCDA), while the POPS continuously measures its sample flow (with a nominal value of approximately 0.181 lpm), and the data processing accounts for this flow variability. Consequently, wind speed effects on the inlet are expected to be more evident in CPC and mCDA data. Based on these flow rates and the inlet diameters (see Sect. S1), the corresponding inlet flow velocities are approximately 0.93 $\mathrm{m\,s^{-1}}$, 0.96 $\mathrm{m\,s^{-1}}$, and 0.93 $\mathrm{m\,s^{-1}}$ for the CPC, POPS, and mCDA, respectively. For the CPC and POPS, which have horizontal inlets, horizontal wind speeds exceeding inlet flow velocities will lead to sub-isokinetic sampling, causing overestimation of larger particles (see Sect. S1 for details). As the horizontal wind was averaging approximately 6.8 $\mathrm{m\,s^{-1}}$ (measured at Sammaltunturi station, Backman et al. (2025)) throughout the whole campaign, sub-isokinetic sampling is expected to occur frequently during the campaign.

Here, we present two cases with two different wind conditions. In the first case, on 22$^{\text{th}}$ September 2022, the horizontal wind speeds are low, at around 2–3 $\mathrm{m\,s^{-1}}$ below 500 m height, as indicated by the Doppler lidar data (Tukiainen et al., 2025) in Fig .S13. Figure S14 presents the measured sample flow rates and total particle number concentrations for this date. As shown in Fig. S14b, the POPS flow rate exhibits significant fluctuations during instrument startup on the ground and in the early stage of ascent. As the payload rises, however, the flow stabilizes. This initial variability is likely due to the POPS pump startup and initial disturbances from the attachment of the payload to the balloon tether line, as well as a short period of the POPS pump malfunctioning that produced erroneous data on the subsequent days between 23$^{\text{th}}$ and 30$^{\text{th}}$ September. As the payload ascends and becomes more stable, the POPS flow correspondingly stabilizes and remains steady up to height exceeding 1 km above the surface.

Figure S14c shows the total particle number concentrations measured by the CPC, POPS, and mCDA. Because these instruments operate over different particle size ranges: 0.01–1 $\mu\mathrm{m}$ for CPC, 0.12–3.4 $\mu\mathrm{m}$ for POPS, and 0.6–41.84 $\mu\mathrm{m}$ for mCDA; their reported total concentrations differ in magnitude. Nevertheless, all three instruments exhibit closely matching temporal trends. Given that the mCDA, with its vertical inlet, is expected to be relatively insensitive to payload orientation, the strong agreement in trends suggests that the CPC and POPS measurements are also stable. A closer examination of the first 10 minutes of data (Fig. S15) reveals no systematic harmonic variation in CPC or POPS concentrations due to inlet orientation. Notably, this period also exhibits the largest POPS flow variability, reaching up to 10 $\mathrm{cm^3\,s^{-1}}$, indicating that these fluctuations were adequately accounted for in the concentration calculations.

Figure S16 shows the averaged particle size distributions (dN/dlogDp) from the mCDA (with vertical inlet) and POPS (with horizontal inlet) over selected 5-minute intervals on 22$^{\text{th}}$ September 2022. The measured distributions are in close agreement throughout these periods. Since the mCDA measurements are largely unaffected by the payload orientation and horizontal wind, this consistency further suggests that the POPS is only minimally influenced by these factors.

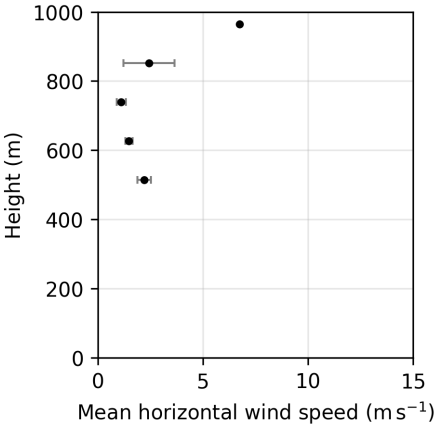

Figure S13. Wind speed obtained from Halo Doppler lidar 2022-09-22 09:00 to 10:00 UTC.

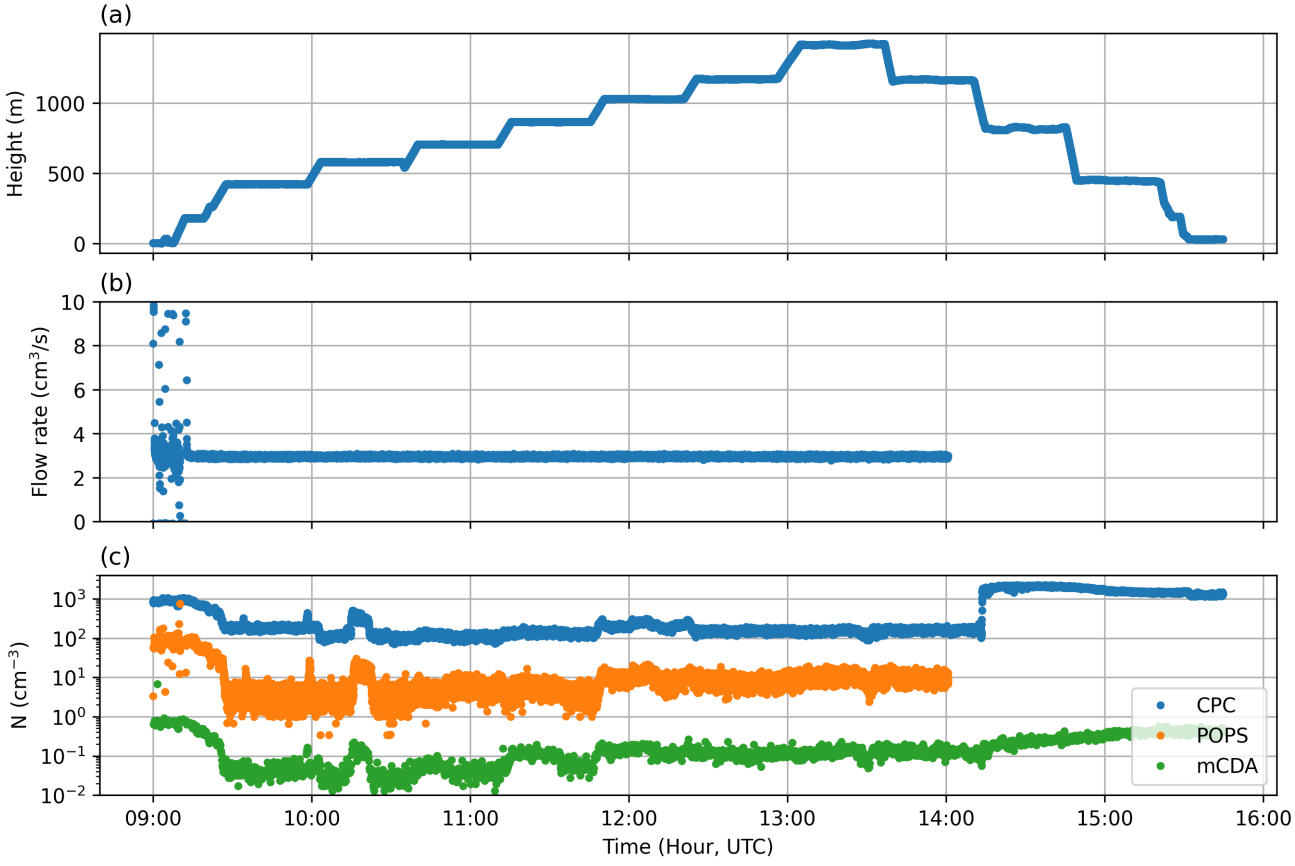

Figure S14. Measurements from the FMI payload on 2022-09-22. a) Payload height relative to the ground, b) Sample flow rate measured by POPS, c) Total particle number concentration from CPC, POPS and mCDA (all bins, PSL equivalent).

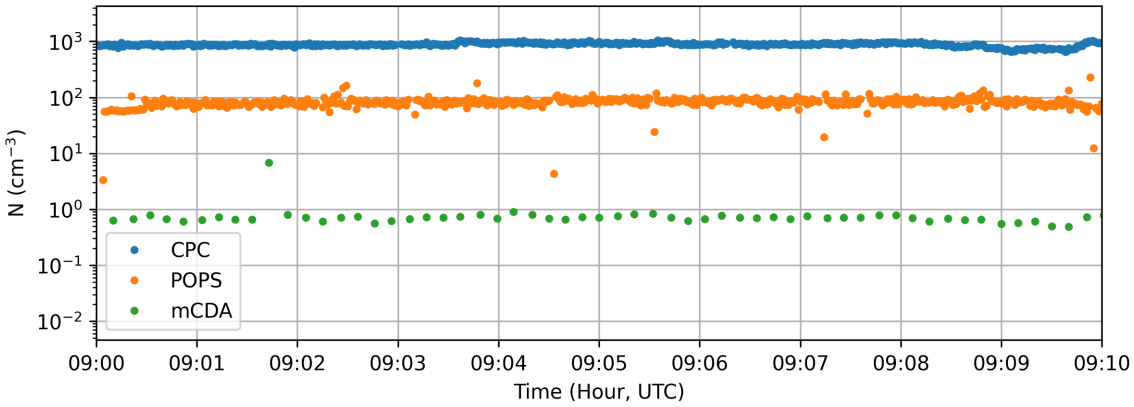

Figure S15. Total particle number concentrations from CPC, POPS, and mCDA (all bins, PSL-equivalent) measured by the FMI payload between 09:00 and 09:10 UTC on 22 September 2022.

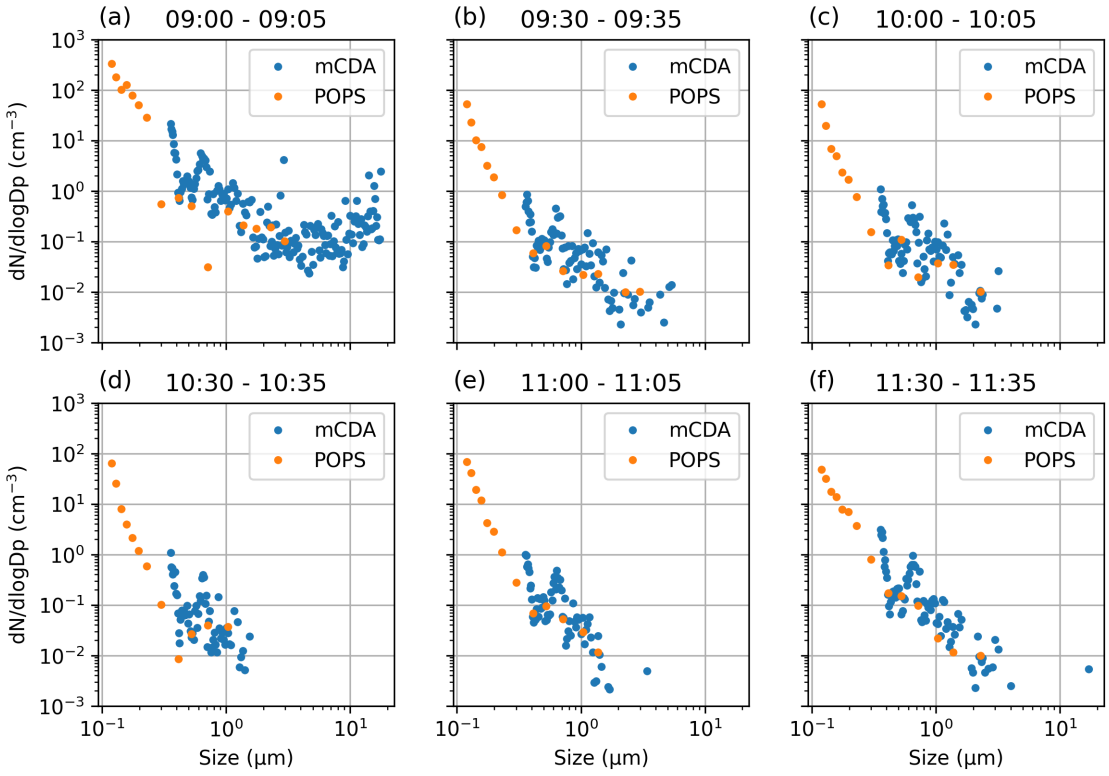

Figure S16. Particle number size distributions (dN/dlogDp) from POPS and mCDA (all bins, PSL-equivalent diameters) measured by the FMI payload on 22 September 2022 over selected 5-minute intervals. The time is in UTC and the selected time intervals are out-of-clouds measurements.

In the second case on 20th September 2022, the horizontal wind speed is high, at around 10–15 $\mathrm{m\,s^{-1}}$ below 500 m height, as seen from the Doppler lidar data (Tukiainen et al., 2025) in Fig .S17. Figure S18 presents the measured sample flow rates and total particle number concentrations for this day. In contrast to the previous case, the POPS flow rate (Fig. S18b) exhibits no significant fluctuations and its variability remains consistent as the payload rises.

Figure S18c shows the total particle number concentrations measured by the CPC, POPS, and mCDA across their respective size ranges. Once again, all three instruments exhibit closely matching temporal trends when the payload outside precipitation period (around 08:30 UTC and 10:00 UTC). Similar to the first case, a closer examination of the data (Fig. S19), when the payload is at 500 m height during horizontal wind speeds exceed 10 $\mathrm{m\,s^{-1}}$, reveals no systematic harmonic variation in CPC or POPS concentrations due to inlet orientation.

Figure S20 shows the averaged particle size distributions (dN/dlogDp) from the mCDA (with vertical inlet) and POPS (with horizontal inlet) over selected 5-minute intervals on 20th September 2022 outside precipitation period. The distributions are in close agreement throughout these intervals. Since the mCDA measurements are largely unaffected by the payload orientation and horizontal wind, this consistency again suggests that the POPS is only minimally influenced by these factors.

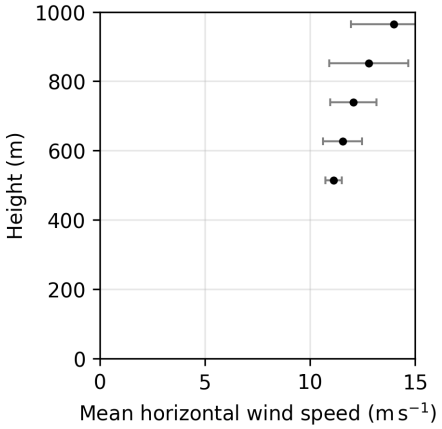

Figure S17. Wind speed obtained from Halo Doppler lidar 2022-09-20 07:00 to 08:00 UTC.

In summary, despite the horizontal inlets of the CPC and POPS, their measurements, both total number concentration and size distribution, agree well with those from the vertically oriented mCDA under both low and high wind conditions with no precipitation. This suggests that inlet orientation and wind have only a minimal influence on the dataset (as the effect of wind is expected to be more pronounced for the POPS and CPC than for the mCDA). Additionally, while the POPS flow rate can fluctuate (for example, during initial instrument setup), these variations were properly accounted for in the concentration calculations. We also observed that precipitation can occasionally affect the POPS flow when large droplets obstruct the inlet, resulting in fluctuation of the flow, such as on 19th September 2022 and 2nd October 2022. However, because flow rate variations are accounted for, these effects should only have minor impact on the POPS data.

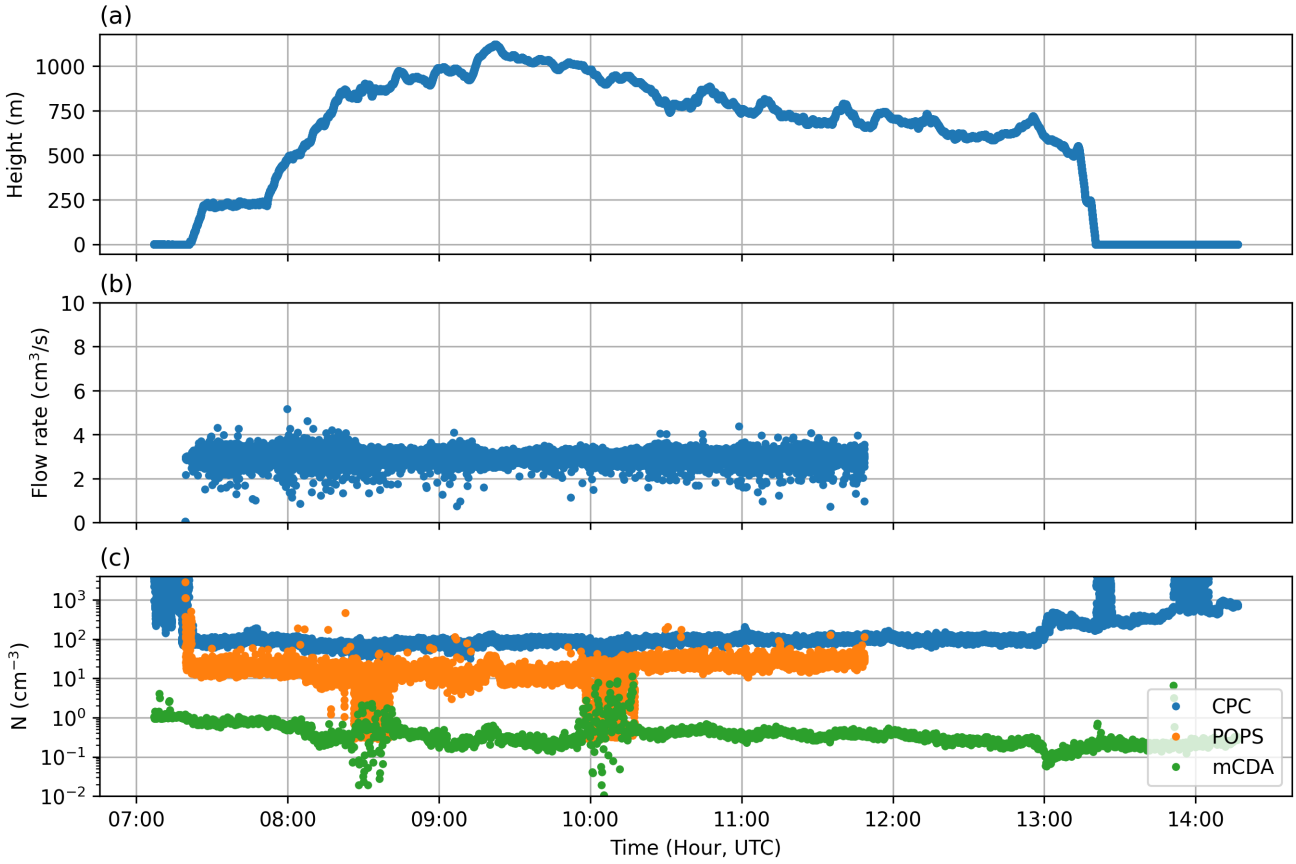

Figure S18. Measurements from the FMI payload on 2022-09-20. a) Payload height relative to the ground, b) Sample flow rate measured by POPS, c) Total particle number concentration from CPC, POPS and mCDA (all bins, PSL equivalent).

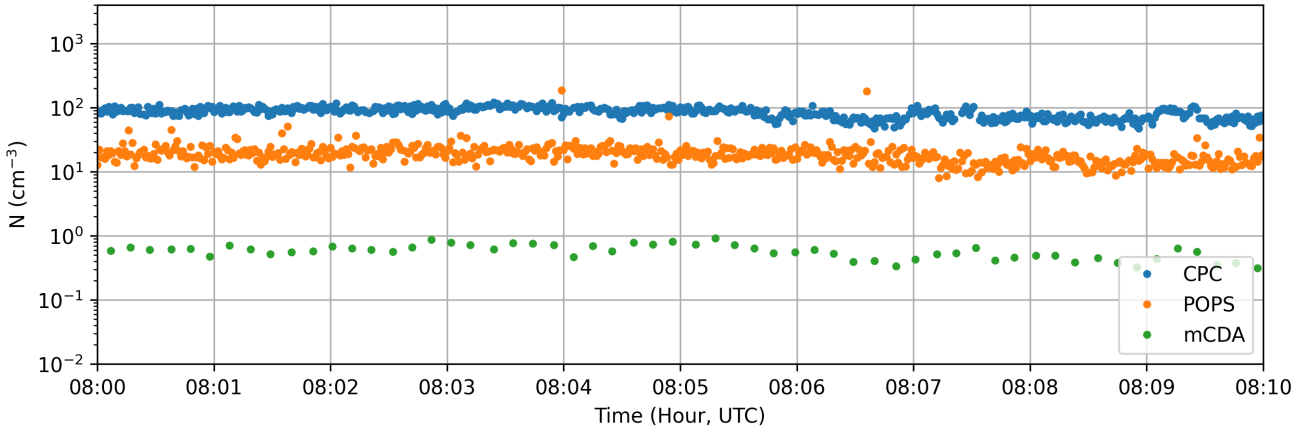

Figure S19. Total particle number concentrations from CPC, POPS, and mCDA (all bins, PSL-equivalent) measured by the FMI payload between 08:00 and 08:10 UTC on 20 September 2022.

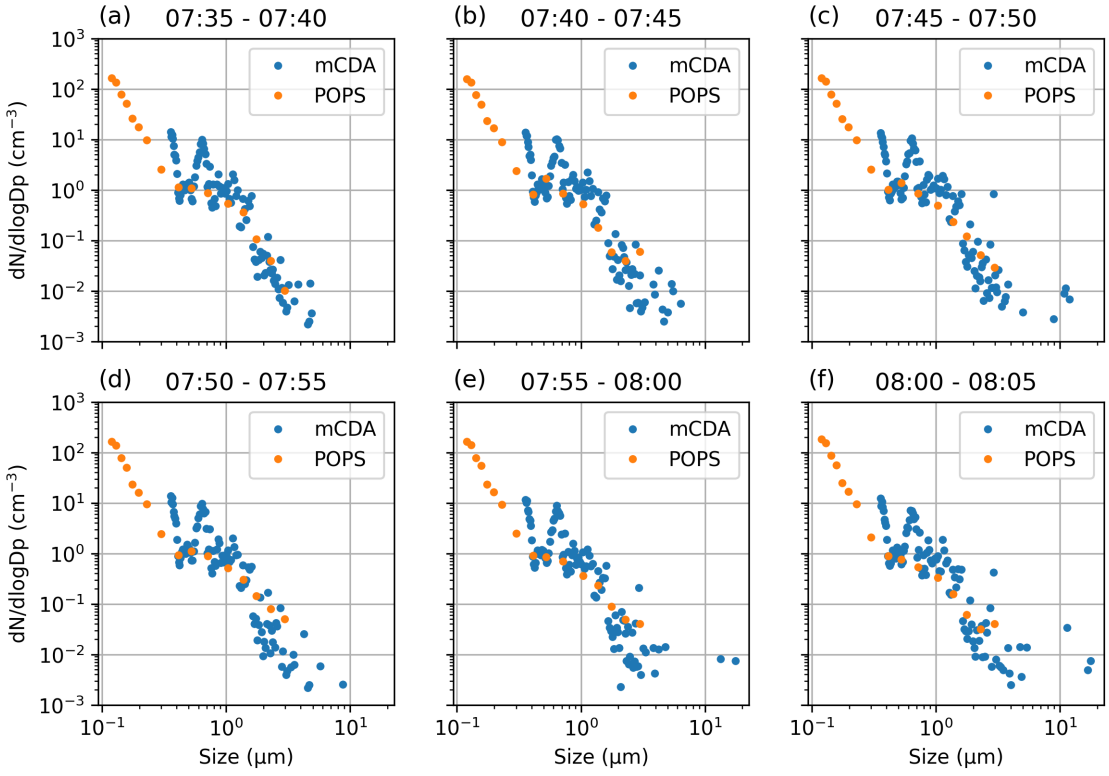

Figure S20. Particle number size distributions (dN/dlogDp) from POPS and mCDA (all bins, PSL-equivalent diameters) measured by the FMI payload on 20 September 2022 over selected 5-minute intervals. The time is in UTC and the selected time intervals are out-of-clouds measurements.

S8 Effects of gasoline winch emissions

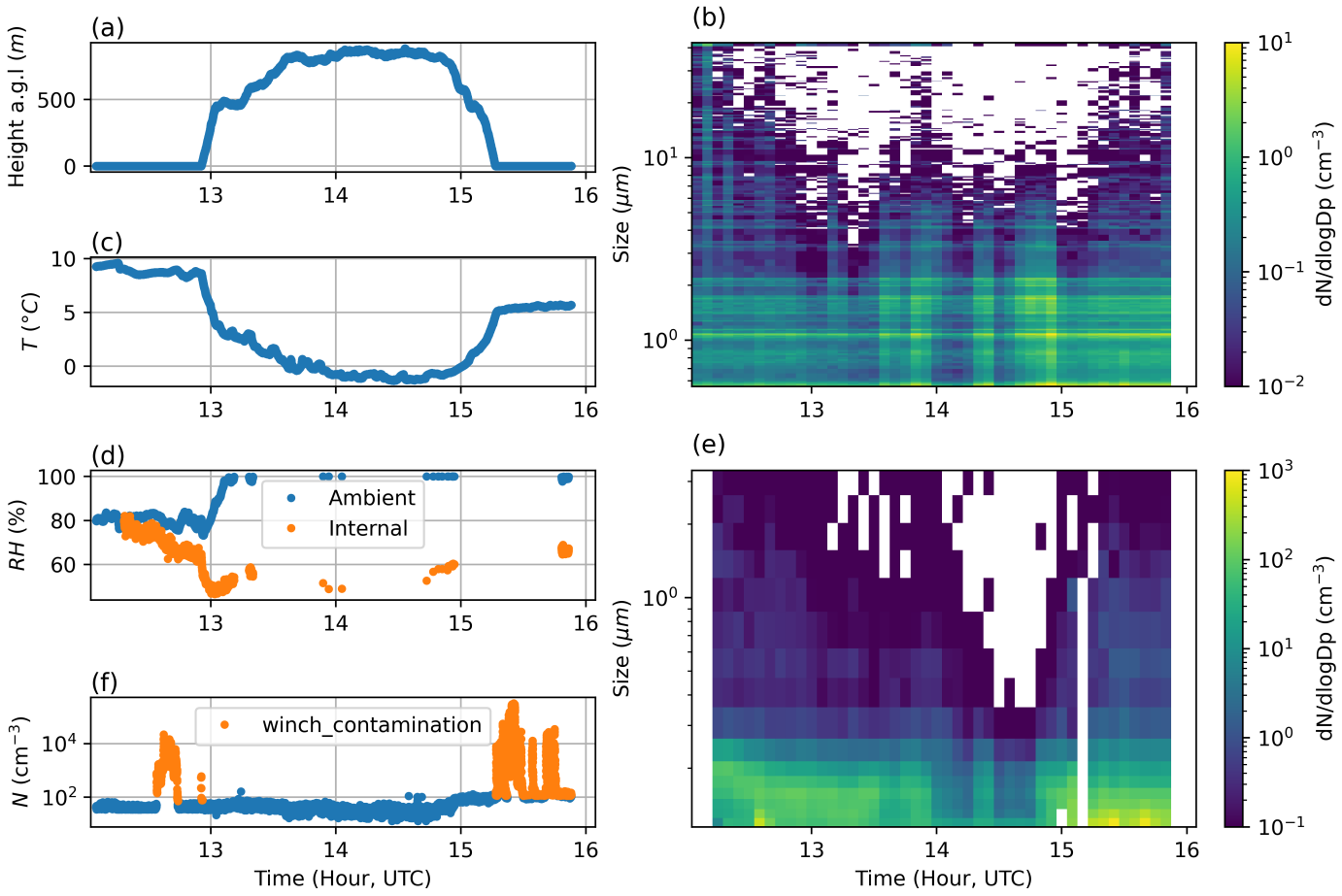

Figure S21. Measurements on the 19th of September flight from the FMI's payload. a) Height above ground level (m), b) dN/dlogD$_p$ (cm^{-3}) calculated from mCDA measurements, c) Temperature (°C) measured by BME280, d) Ambient relative humidity (%) measured by BME280 and calculated internal relative humidity, e) dN/dlogD$_p$ (cm^{-3}) calculated from POPS measurements and f) Number concentration (cm^{-3}) from CPC with the `winch_contamination` flag. Subplots (b) and (e) are averaged over 5 minutes for visualization.

For flights conducted during the first two weeks of the campaign (16th–28th September), a gasoline winch was used to control the height of the balloon. Although the gasoline winch operates intermittently, only during ascent and descent of the payload, it may still influence the particle measurements from POPS and CPC to some extent. However, such contamination is clearly distinguishable, as it is typically orders of magnitude higher than background concentrations. Such example is shown in Fig. S21, particularly before and at the start of takeoff around 13 UTC, and after landing around 15:15 UTC. During these periods, sharp peaks in number concentration, sometimes up to two orders of magnitude higher, can be attributed

to gasoline emissions. These intervals were therefore flagged as periods of enhanced number concentration associated with gasoline contamination.

Gasoline emissions typically exhibit a bimodal particle size distribution (Raza et al., 2018), consisting of a nucleation mode (< 50 nm) and an accumulation mode (50–200 nm). Given the measurement ranges of the instruments (0.01–1 μm for CPC and 0.12–3.4 μm for POPS), CPC total number concentration was used to identify winch-related contamination in the dataset. An interquartile range (IQR) filtering method was applied to detect spikes in CPC particle number concentration below 100 m altitude. Specifically, the first (Q1) and third (Q3) quartiles were calculated, and the IQR defined as $Q3 - Q1$. Data points exceeding $Q3 + 1.5 \times \mathrm{IQR}$ were classified as invalid and assigned a `winch_contamination` flag value of 1. The dataset was carefully inspected on a case-by-case basis to ensure that no residual contamination spikes remain.

Treating the gasoline winch emissions as a point source, we further assess its influence on the FMI payload measurements by simulating both the initial plume rise and the subsequent atmospheric dispersion using a Gaussian plume model (Seinfeld and Pandis, 2016). Because the exhaust from the gasoline engine is substantially hotter than the ambient air, the plume rises due to combined buoyancy and momentum effects. The plume rise is calculated following Briggs' approach (Briggs, 1969), using an exhaust temperature of 600 K, ambient temperature of 280 K, exit velocity of 20 m s^{-1}, and exhaust diameter of 0.05 m.

To account for atmospheric diffusion, a Gaussian plume dispersion model (Turner, 1969; Seinfeld and Pandis, 2016) is applied under a worst-case scenario of extremely unstable atmospheric conditions (Pasquill–Gifford stability class A; (Pasquill, 1971; Seinfeld and Pandis, 2016)), corresponding to strong vertical mixing. Two wind scenarios are considered: low wind (1 m s^{-1}) and high wind (10 m s^{-1}).

As shown in Fig. S22 and Fig. S23, concentrations decrease rapidly with both distance from the source and height above ground in both conditions. Compared to high wind conditions (Fig. S23), low wind conditions (Fig. S22) are characterized by weaker horizontal advection and unsuppressed vertical mixing, resulting in relatively higher concentrations near the source and at elevated heights. At lateral distances of 50 m and 100 m from the plume centerline (Fig. S22b and Fig. S23b), concentrations also decrease by several orders of magnitude compared to right at the plume centerline.

Since the tethered balloon system operates at an inclination angle greater than 45° relative to the ground, the relative concentrations due to gasoline emission is significantly smaller compared to the source. For example, at the plume centerline at 100 m downwind and 100 m height above ground, the relative concentration compared to the source is 3×10^{-12} under low wind conditions, compared to 3×10^{-13} under high wind conditions. Given that the exhaust emission is only approximately two orders of magnitude higher than background levels (as observed when the payload is on the ground near the winch; Fig. S21), the contribution of gasoline emissions becomes negligible relative to the background when the payload is at 100 m height above ground level.

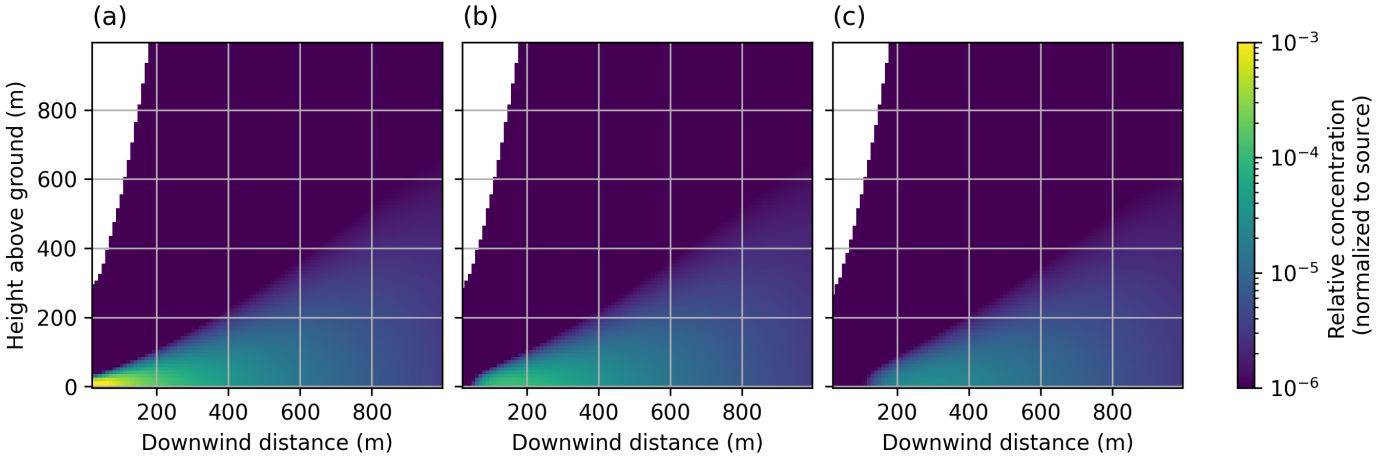

Figure S22. Gaussian plume dispersion modelling of gasoline engine emissions during low wind condition (1 m s^{-1}). The panels present the relative concentration, normalized to the source concentration, as a function of height above ground and downwind distance. The results are shown for (a) the plume centerline, (b) 50 m lateral distance from the centerline, and (c) 100 m lateral distance from the centerline.

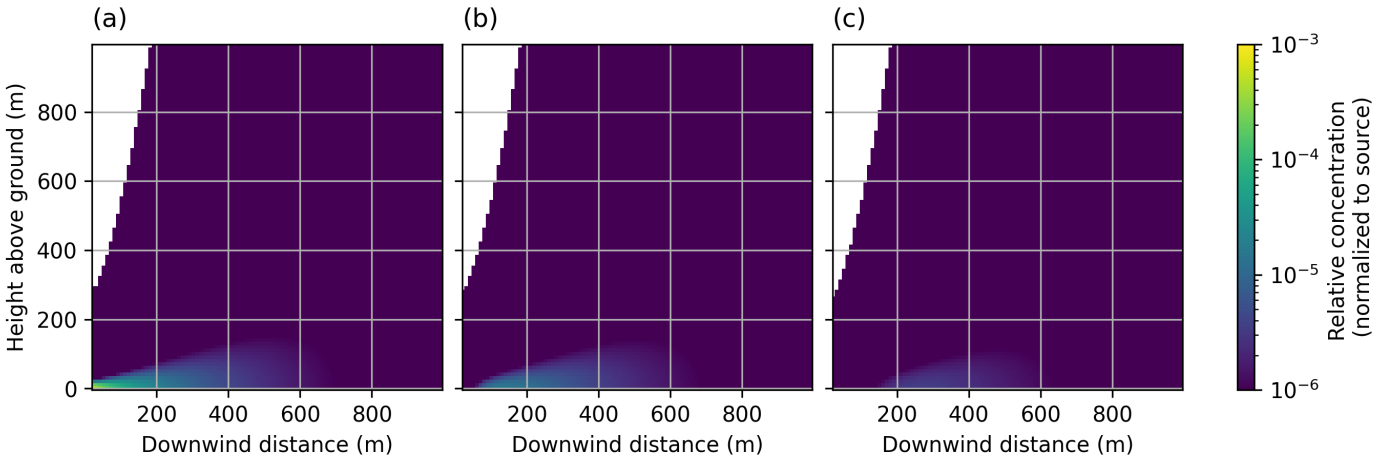

Figure S23. Gaussian plume dispersion modelling of gasoline engine emissions during high wind condition (10 m s^{-1}). The panels present the relative concentration, normalized to the source concentration, as a function of height above ground and downwind distance. The results are shown for (a) the plume centerline, (b) 50 m lateral distance from the centerline, and (c) 100 m lateral distance from the centerline.

References

Backman, J., Luoma, K., Servomaa, H., Vakkari, V., and Brus, D.: In-situ aerosol measurements at the Arctic Sammaltunturi measurement station during the Pallas Cloud Experiment 2022, Earth System Science Data Discussions, pp. 1–22, https://doi.org/10.5194/essd-2025-284, 2025.

Briggs, G. A.: Plume rise, TID-25075, 1969.

Doulgeris, K.-M., Komppula, M., Romakkaniemi, S., Hyvärinen, A.-P., Kerminen, V.-M., and Brus, D.: In situ cloud ground-based measurements in the Finnish sub-Arctic: intercomparison of three cloud spectrometer setups, Atmospheric Measurement Techniques, 13, 5129–5147, https://doi.org/10.5194/amt-13-5129-2020, publisher: Copernicus GmbH, 2020.

Doulgeris, K. M., Kaikkonen, V., Juttula, H., Molkoselkä, E., Mäkynen, A., and Brus, D.: In situ surface cloud measurement dataset from four cloud spectrometers during the Pallas Cloud Experiment (PaCE) 2022, Earth System Science Data, 17, 6497–6506, https://doi.org/10.5194/essd-17-6497-2025, 2025.

Doulgeris, K. M., et al, and et al: Evaluation of cloud spectrometers and one holographic imaging probe during the Aerosol, Clouds and Trace Gases Research Infrastructure (ACTRIS) cloud in situ intercomparison campaign under sub-zero conditions at Sonnblick Observatory., submitted to Atmos. Meas. Tech, 2026.

Pasquill, F.: Atmospheric dispersion of pollution, Quarterly Journal of the Royal Meteorological Society, 97, 369–395, https://doi.org/https://doi.org/10.1002/qj.49709741402, _eprint: https://rmets.onlinelibrary.wiley.com/doi/pdf/10.1002/qj.49709741402, 1971.

Raza, M., Chen, L., Leach, F., and Ding, S.: A Review of Particulate Number (PN) Emissions from Gasoline Direct Injection (GDI) Engines and Their Control Techniques, Energies, 11, 1417, https://doi.org/10.3390/en11061417, publisher: Multidisciplinary Digital Publishing Institute, 2018.

Seinfeld, J. H. and Pandis, S. N.: Atmospheric chemistry and physics: from air pollution to climate change, John Wiley & Sons, New York, ISBN 1-118-94740-1, 2016.

Tukiainen, S., Siipola, T., Leskinen, N., and O'Connor, E.: Remote sensing measurements during PaCE 2022 campaign, Earth System Science Data, 17, 3797–3806, https://doi.org/10.5194/essd-17-3797-2025, 2025.

Turner, D. B.: Workbook of Atmospheric Diffusion Estimates, USEPA 999-AP-26, U.S. Environmental Protection Agency, Washington, DC, 1969.

von der Weiden, S.-L., Drewnick, F., and Borrmann, S.: Particle Loss Calculator – a new software tool for the assessment of the performance of aerosol inlet systems, Atmospheric Measurement Techniques, 2, 479–494, https://doi.org/10.5194/amt-2-479-2009, 2009.